ACCSCIENCE PUBLISHING

Materials Science in Additive Manufacturing

ORIGINAL RESEARCH ARTICLE

Design and characterization of additively manufactured energy-absorbing mechanical metamaterials with bioinspired geometries

Eduard Farber*, Alexey Orlov, and Anatoliy Popovich

Institute of Machinery, Materials, and Transport, Peter the Great St. Petersburg Polytechnic University, Saint Petersburg, Russia

(This article belongs to the *Special Issue: Advances in Tailoring of Microstructure, Materials, and Design with Additive Manufacturing*)

Abstract

One of the most promising and innovative approaches in designing mechanical metamaterials for various applications is the use of bioinspired geometries. Nature offers a wide array of geometric forms and structures that have evolved to serve specific functions, including protection. Examples of such structures include the microstructure of pomelo peels and the geometry of starfruits (carambola), both of which are designed to protect the fruit from impact when falling from a height. Based on these natural structures, it is possible to develop metamaterials that exhibit low weight, high strength, and enhanced energy absorption properties. Furthermore, additive manufacturing technologies enable the fabrication of such metamaterials with unit cell geometries of arbitrary complexity. In this study, the microstructures of pomelo peels and the forewing of the Japanese rhinoceros beetle were used as source geometries for the design of metamaterials. Metamaterial specimens, consisting of 5 × 5 × 5-unit cells with an initial model porosity of 80%, were fabricated from Ti6Al4V alloy using the selective laser melting method. Quasi-static and dynamic compression tests were conducted to determine the mechanical properties and specific energy absorption of the metamaterials. The compressive yield strength of the metamaterial samples based on the Japanese rhinoceros beetle forewing microstructure was 134 MPa, compared to 115.87 MPa for those based on the pomelo peel microstructure. Under quasi-static compression, the energy absorption level of the metamaterial samples based on the rhinoceros beetle wing microstructure was 13.83 J, with a specific energy absorption of 4.61 J/g. The results demonstrate the overall promise of employing a bioinspired approach for designing energy-absorbing metamaterials. These findings will serve as a basis for further in-depth research and development of energy-absorbing systems and components based on the geometries presented in this work.

Keywords: Mechanical metamaterials; Energy absorption; Selective laser melting; Bioinspired design; Mechanical characterization; Finite element method

***Corresponding author:**
Eduard Farber
(d.farber2010@yandex.ru)

Citation: Farber E, Orlov A, Popovich A. Design and characterization of additively manufactured energy-absorbing mechanical metamaterials with bioinspired geometries. *Mater Sci Add Manuf*. 2026;5(2):025360082. doi: 10.36922/MSAM025360082

Received: September 3, 2025

Revised: October 13, 2025

Accepted: October 22, 2025

Published online: March 11, 2026

1. Introduction

There is a growing demand for lightweight structures and components with enhanced strength and energy-absorption characteristics for use in various energy-absorbing

devices.[1-3] Such devices are widely employed in the automotive, aerospace, defense, and other industries to protect and dissipate kinetic energy in emergency impact scenarios.[4-6] To improve the properties of these devices, extensive research is being conducted, primarily focusing on the use of mechanical metamaterials with different unit cell geometries to achieve optimal performance.[6-8] As is known, mechanical metamaterials are artificially engineered materials with specific geometries and arrangements of unit elements (unit cells), designed to exhibit unique properties such as a negative Poisson's ratio or high-specific energy absorption.[7,9-14] Accordingly, it is clear that the properties of mechanical metamaterials are primarily determined by the geometry or topology of their unit elements.[10,11,15] One promising research direction in this field is the development of bioinspired geometries, using or adapting structures found in living organisms.[16-20] This approach combines modern scientific and technological capabilities, particularly additive manufacturing, with evolutionary solutions that provide the best adaptation mechanisms for living beings to their environments.[16,21-23] Depending on the research objectives, the source biological geometries may include deep-sea sponge skeletal structures,[8,24,25] pomelo peels,[7] honeycomb patterns,[5,26] crab exoskeletons,[27] cacti,[28] microstructure of mammalian (dog) paw pads,[29] starfruit (carambola) geometry,[30] mantis shrimp claw structure,[16] and others.[21] In some cases, geometries are combined,[4] such as hybrid designs of honeycombs and hierarchical human bone structures,[2] honeycombs and pomelo peel structures,[31] or human spinal column and turtle shell structures.[32] Additive manufacturing technologies, such as material extrusion, powder bed fusion, and others, play a crucial role in enabling and implementing such research. They allow the fabrication of highly complex geometries from various materials, including polymers, metals, and alloys.[8,21,33-36] These studies and the utilized geometries clearly demonstrate the promising potential and active research in applying bioinspired designs to create energy-absorbing structures. It is also worth emphasizing the need for further research in this field, particularly in the context of designing bioinspired metamaterials.

As previously mentioned, one of the primary factors influencing the properties of mechanical metamaterials is the geometry of their unit cells. Consequently, the most effective design approach appears to be the use of symmetric or partially symmetric structures. Such structures are ideally suited for defining the topology of a unit cell, which can then be replicated into an array – that is, a metamaterial sample with the specified topology. Examples of such structures can be found in the study by Zhang *et al*.,[7] where a 4 × 4 × 4 mm unit cell was designed based on pomelo peels. The authors reported a notably high energy absorption performance. In addition, reference should be made to Du *et al*.,[37] who introduced a geometry inspired by the microstructure of the Japanese rhinoceros beetle's forewing. It was noted that this geometry, fabricated from an aluminum alloy, exhibits mechanical properties comparable to those of titanium alloy structures. Consequently, additional research is required to explore the potential of these geometrical designs in creating mechanical metamaterials with optimized energy absorption performance.

Based on the considerations mentioned above, we aim to design mechanical metamaterials incorporating the geometrical configurations described in previous studies.[7,37] The design process of unit cells and metamaterial samples involves numerical computer simulation to conduct preliminary evaluations of the metamaterials' properties, with particular emphasis on the influence of unit cell porosity levels. Specimen fabrication was accomplished through selective laser melting (SLM) using Ti6Al4V alloy powder, followed by experimental testing to determine key performance characteristics and validate the simulation results. The implementation of this combined "simulation-experimentation" approach is expected to streamline and accelerate the development and design process of mechanical metamaterials. This is achieved by enabling more accurate performance predictions during the design phase through numerical computer simulation. This study compares the efficiency of the two investigated geometries and assesses their potential application in designing mechanical metamaterials with enhanced energy-absorption properties, paving the way for further development of structures and components based on these geometries.

2. Materials and methods

2.1. Materials

The metamaterial samples and the solid alloy samples, necessary to determine their baseline properties for numerical simulation, were fabricated from spherical Ti6Al4V alloy powder. The chemical composition of the source powder is presented in Table 1. The solid alloy samples possessed the following geometric parameters: d = 3 mm, h = 13 mm for compression to failure tests, d = 10 mm, h = 90 mm to determine elastic modulus, d = 6 mm (working section), h = 63 mm for tensile tests, d = 5.7 mm (working section), and h = 53 mm for torsion tests. The samples were fabricated using a 3DLAM Mini SLM system (3DLAM Company, Russia) in an inert argon atmosphere. The system is equipped with an IPG Photonics (United States) fiber laser. The build

chamber is cylindrical with a diameter of 90 mm and a height of 100 mm. The following processing parameters were used: laser power: 150 W, scanning speed: 1200 mm/s, hatch spacing: 0.12 mm, layer thickness: 0.03 mm, and spot diameter: 0.08 mm. The metamaterial samples were oriented horizontally during manufacturing, as shown in Figure 1. The samples were fabricated according to the original models with 80% porosity. Following fabrication, all samples underwent heat treatment in a vacuum at a temperature of 1,050°C for 120 min, followed by furnace cooling.

2.2. Finite element modeling and mechanical characterization

The geometric models of the unit cells and metamaterial samples were created and numerically simulated using the finite element analysis package ANSYS 2019 R2 SpaceClaim (ANSYS 2019 R2, Ansys Inc., United States). The unit cell dimensions were 2.5 × 2.5 × 2.5 mm. The metamaterial samples comprised a 5 × 5 × 5 array of unit cells, resulting in a total of 125 cells, with overall dimensions of 12.5 × 12.5 × 12.5 mm. Two unit cell models were prepared: Strut_06 (hereinafter referred to as S06), based on the geometry from Zhang *et al.*,[7] and Strut_08 (hereinafter S08), based on the geometry from Du *et al.*[37] The topologies of the S06 and S08 unit cells, featuring 80% porosity, are presented in Figure 2. The metamaterial samples constructed based on these topologies are shown in Figure 3.

Next, the ANSYS 2019 R2 SpaceClaim software package (version 2019.2.0.04089) was used to determine the mechanical characteristics of the metamaterials—Young's modulus (E), yield strength, and compressive strength—by simulating a compression experiment with static load in both elastic and plastic regions using the finite element method. To determine the Young's modulus, the following boundary conditions were applied: normal displacement without friction was applied on the lower face, and a small displacement corresponding to 0.01% strain was used on the upper face of the metamaterial samples. To determine the compressive yield strength and ultimate compressive strength, analogous boundary conditions were applied, with a level of displacement corresponding to 5% strain.

2.3. Mechanical testing and energy absorption characterization

Visual inspection of the fabricated metamaterial samples was conducted using a TESCAN Mira 3 LMU scanning electron microscope (SEM) (TESCAN, Czech Republic) in a secondary electron mode. Quasi-static compression tests to failure and tensile tests, conducted on both solid alloy and metamaterial samples, were performed using a Zwick/Roell Z100 uniaxial testing machine. Torsion tests of solid samples, as well as dynamic compression tests (impact) to failure of the metamaterial samples, were performed on a Gleeble 3800 system (Dynamic Systems Inc., United States). During dynamic testing, the compression rate was 0.7 m/s.

Table 1. Chemical composition of Ti6Al4V (wt. %)

Chemical	Titanium	Aluminum	Vanadium	Iron	Oxygen	Carbon	Nitrogen	Hydrogen	Other
Max	Balance	6.4	3.8	0.3	0.12	0.06	0.03	0.011	0.09

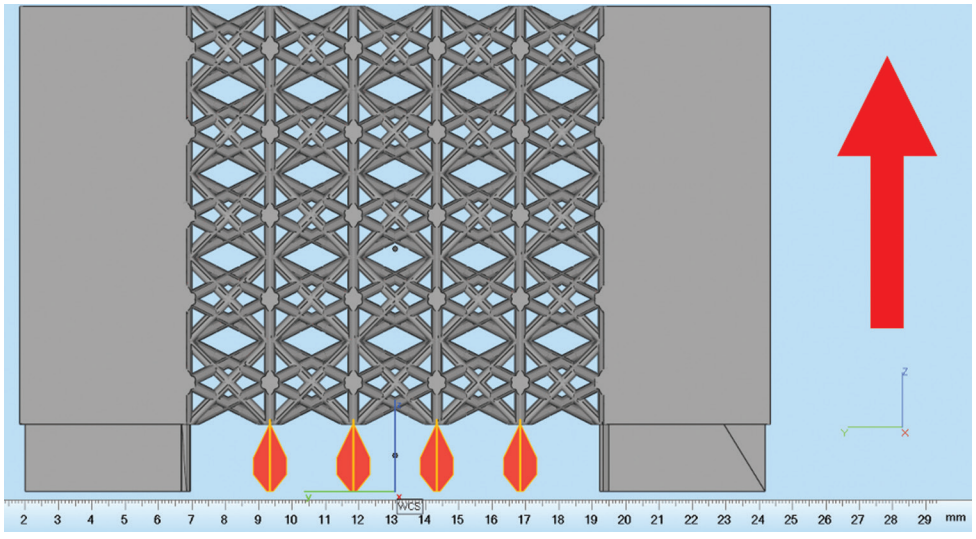

Figure 1. Orientation of the metamaterial sample on the build plate, with the building direction indicated by the arrow

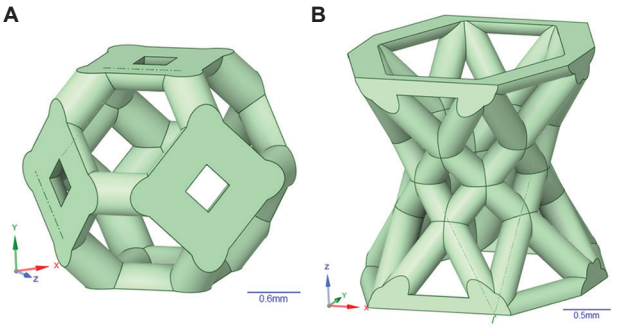

Figure 2. Unit cell topologies. (A) Strut_06. Scale bar: 0.6 mm. (B) Strut_08. Scale bar: 0.5 mm

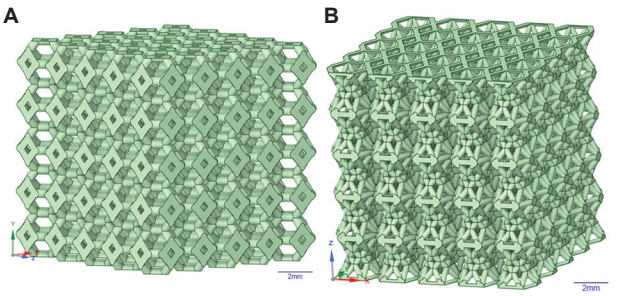

Figure 3. Models of the metamaterial samples. (A) Strut_06. (B) Strut_08

The porosity of the fabricated metamaterial samples was calculated using Equation (1):[38,39]

$$P = (1 - \frac{\rho^*}{\rho_s}) \quad (1)$$

where ρ^* is the density of the metamaterial sample and ρ_s is the density of the material from which the metamaterial sample was fabricated.

To evaluate the energy absorption of the investigated metamaterial samples, several metrics were calculated. The fundamental energy absorption (EA) metric was determined by mathematically integrating the load-displacement curve, which can be expressed using Equation (2):[5]

$$EA = \int_0^x F(x)dx \quad (2)$$

Specific energy absorption (SEA) was used to evaluate the energy absorption efficiency per unit mass of the investigated structure and was calculated using Equation (3):[31]

$$SEA = \frac{EA}{m} \quad (3)$$

where m is the mass of the structure of the metamaterial sample.

2.4. Statistical analysis

For each test, three metamaterial specimens of each topology were fabricated. In total, 12 specimens were manufactured and tested (six of each topology). Analysis of the obtained results, their processing, and the preparation of the stress–strain curve graphs were performed using the Origin software (version SR1 b9.5.1.195).

3. Results and discussion

3.1. Mechanical characterization of the Ti6Al4V alloy

Based on the testing results of the solid alloy samples, a set of properties that were necessary and sufficient for numerical computer simulation was obtained. The experimentally determined properties of the Ti6Al4V alloy are presented in Table 2.

Figure 4 shows the stress–strain curve obtained from the compression testing of the Ti6Al4V alloy samples, which was imported into the ANSYS 2019 R2 SpaceClaim software package to determine the properties of the metamaterials.

3.2. Effect of porosity on the simulated mechanical properties of S06 and S08 metamaterials

Based on the results of the numerical computer modeling, the values of the elastic modulus (E), compressive yield strength, and ultimate compressive strength of the metamaterial samples with different porosities were obtained. The results are presented in Table 3. The thicknesses of the unit cell struts (T) are also indicated.

For a more comprehensive analysis of the results, Figure 5 presents the dependence of elastic modulus (E), compressive yield strength, and ultimate compressive strength on the porosity of the metamaterials. Based on Figure 5, it can be observed that increasing the porosity of the metamaterial unit cells, by increasing the strut thickness, led to an increase in the values of the resulting metamaterial properties. A nearly linear dependence is observed for all parameters. At the same time, the elastic modulus values obtained through modeling did not differ significantly between the topologies. However, the strut thicknesses of the topologies varied considerably, with this difference increasing as porosity decreased. At 70% porosity, the strut thickness of the metamaterial with topology S06 was 202 μm greater than that of the metamaterial with topology S08. At 65% porosity, the difference in thickness reached 221 μm.

Table 2. Experimentally obtained properties of Ti6Al4V that were used in the simulation

Parameters	Value
Density, ρ (kg/m³)	4,458
Elastic modulus, E (GPa)	155.78
Shear modulus, G (GPa)	59.14
Poisson's ratio, ν	0.317

Table 3. Properties of metamaterial samples with S06 and S08 unit cell topologies, obtained by simulation

Parameters	Porosity (%)	Topology	
		S06	S08
Elastic modulus (GPa)	85	3.92	4.69
	80	7.22	7.46
	75	11.45	11.10
	70	16.59	15.63
	65	22.48	21.24
Yield strength (MPa)	85	32.5	32
	80	55.7	50.3
	75	77.5	72.25
	70	103.4	101.7
	65	130	132.5
Compressive strength (MPa)	85	42.14	40.79
	80	67.48	69.40
	75	94.63	93.51
	70	123.39	131.6
	65	156.43	169.07
Thickness of unit cell struts (μm)	85	416.3	279.7
	80	491	330
	75	560.5	378.6
	70	627	425
	65	691.2	470.2

The compressive strength of the metamaterial with topology S08 was higher than that of the metamaterial with topology S06 for all porosity variants, excluding the 65% porosity data. At 65% porosity, the compressive strength of the metamaterial with topology S08 was higher than that of the metamaterial with topology S06. A similar trend was observed for the yield strength. An inverse relationship was noted for the elastic modulus: at 85% and 80% porosity, the elastic modulus of the metamaterial with topology S06 was lower than that of topology S08. As the porosity decreased to 75% and below, the elastic modulus of metamaterials with topology S06 increased compared to the metamaterials with topology S08.

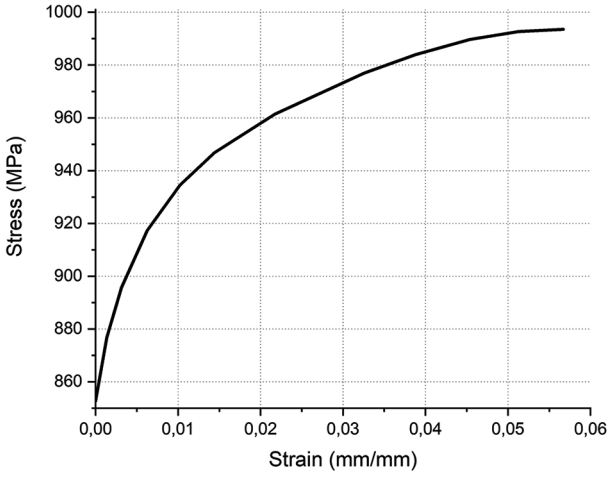

Figure 4. Stress-strain curve of Ti6Al4V alloy used in the simulation

3.3. Experimental characterization and validation of simulated metamaterial properties

Figures 6 and 7 present the SEM images of the fabricated metamaterial samples and their unit cells with topologies S06 and S08, respectively. Powder adhesion to the struts of the unit cells was clearly visible. The porosity of the obtained metamaterial samples was 72.38% for topology S06 and 68.53% for topology S08. The average front-view strut thickness was 497.3 μm for topology S06 and 363.23 μm for topology S08.

Figure 8 presents the X-ray diffraction results of one of the as-fabricated samples. Only the α-titanium phase with a hexagonal close-packed structure was observed. No other phases were detected.

Figure 9 shows the stress–strain curves obtained from the compression tests of metamaterial samples with topologies S06 and S08, respectively. The metamaterial samples after testing are presented in Figures 10 and 11.

From Figure 9, it can be observed that the metamaterial samples with topology S08 are characterized by a greater strain to failure, indicating their higher ductility. The descending segment of the curve suggests gradual failure of the samples without an abrupt load drop. In contrast, the metamaterial samples with topology S06 failed on reaching maximum stress, with a poorly defined plastic deformation region followed by rapid fracture. For both metamaterial topologies, failure occurred at a 45° angle, which is a characteristic of classical materials. In the metamaterial with topology S06 (Figure 10A), the failure line essentially passed through the centers of the unit cells. The cells were fractured, causing the upper part of the sample to shift and become wedged into the lower part. Meanwhile, the

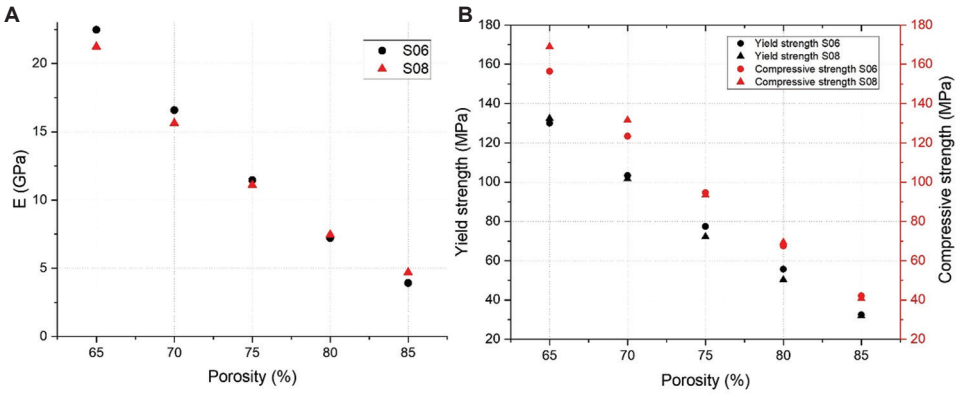

Figure 5. Dependence of metamaterial properties on porosity. (A) Elastic modulus. (B) Compressive yield strength and ultimate compressive strength

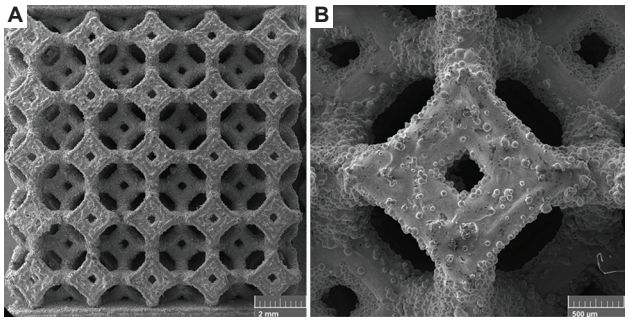

Figure 6. Scanning electron microscopic images of the metamaterial sample with S06 topology, front view. (A) Sample. Scale bar: 2 mm, magnification: ×19. (B) Unit cell. Scale bar: 500 μm, magnification: ×80

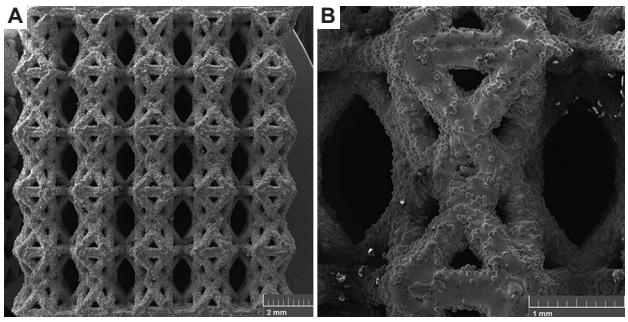

Figure 7. Scanning electron microscopic images of the metamaterial sample with S08 topology, front view. (A) Sample. Scale bar: 2 mm, magnification: ×19. (B) Unit cell. Scale bar: 1 mm, magnification: ×70

cells located outside the failure line, at the edges of the sample, appeared intact, with no visible cracks or damage. In cells situated immediately adjacent to the failure line (Figure 10B), cracks of various sizes were observed on the struts. It should be noted that a similar failure process at a 45° angle has been reported for geometries based on pomelo peels in other research studies.[7,40]

Conversely, Figure 11A shows that the failure line of the metamaterial sample with topology S08 passed through the

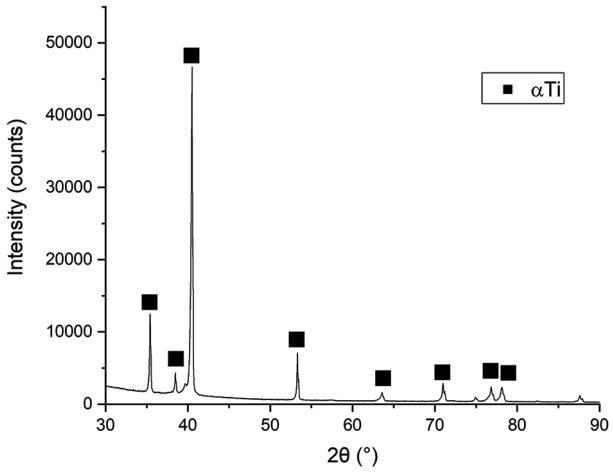

Figure 8. X-ray diffraction pattern of the sample in the as-fabricated and heat-treated conditions

bases of the unit cells. Displacement and partial fracture of the cells were observed, primarily in the region of their bases (Figure 11B). The central parts of the cells remained intact. In cells not located on the failure line (e.g., the top row), cracks were observed on the struts at the cell bases, at the midpoints of the struts, as well as at the points of contact with other struts. Overall, similar failures of struts at the bases of unit cells have been reported by Du *et al.*,[37] where failures were primarily noted at the bases of the structures.

The parameters obtained from the static compression tests to failure for each topology—elastic modulus, conditional yield strength, conditional ultimate compressive strength, and maximum strain of the metamaterial samples—are presented in Table 4.

Based on the data presented in Table 4, it can be observed that the metamaterial samples with topology S08 exhibited superior characteristics compared to those with topology

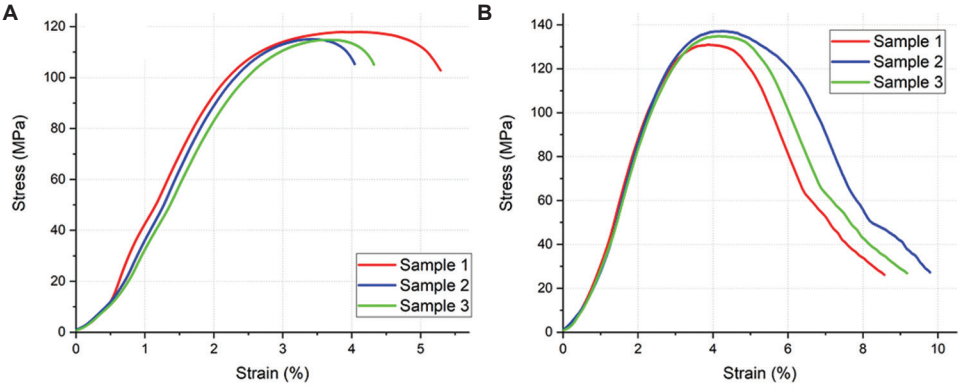

Figure 9. Stress-strain curves of samples under compression. (A) Strut_06. (B) Strut_08

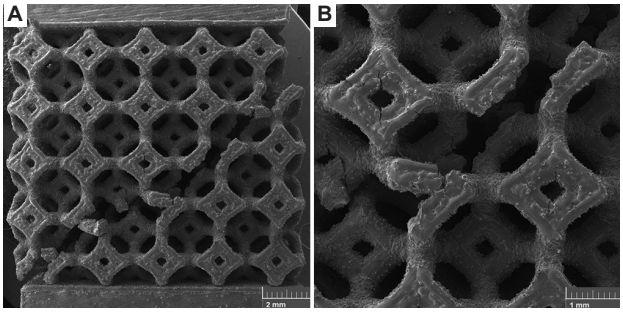

Figure 10. Scanning electron microscopic images of the metamaterial sample with S06 topology after the compression test, front view. (A) Sample. Scale bar: 2 mm, magnification: ×18. (B) Unit cell. Scale bar: 1 mm, magnification: ×40

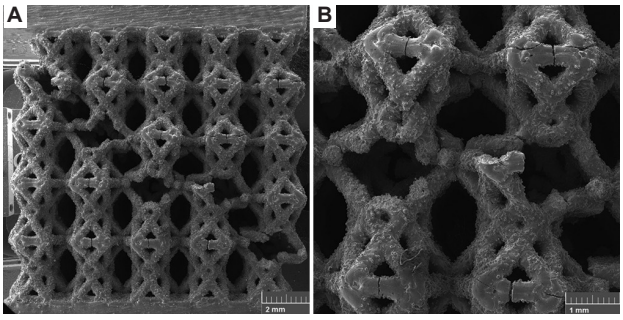

Figure 11. Scanning electron microscopic images of the metamaterial sample with S08 topology after the compression test, front view. (A) Sample. Scale bar: 2 mm, magnification: ×18. (B) Unit cell. Scale bar: 1 mm, magnification: ×40

S06. Specifically, topology S08 was characterized by a higher elastic modulus (6.44 GPa on average), an ultimate compressive strength averaging 134 MPa, and maximum strain values (9.18% on average). For the metamaterial sample with topology S06, the ultimate compressive strength was 115.87 MPa. A relatively high level of result reproducibility was noted for both metamaterial unit cell topologies.

Compared to literature data, the obtained values of elastic modulus, yield strength, and compressive strength for the metamaterial with topology S06 were higher than those reported in other studies[7,40] on metamaterials with pomelo peel-based geometries. This is attributed to the lower porosity of the fabricated S06 topology metamaterial samples compared to the original models. It should also be noted that in Zhang *et al.*,[40] the sample porosity was 92%, which naturally led to reduced mechanical properties of the samples.

Furthermore, the modeling and experimental results were compared. For greater clarity, Table 5 presents a comparison of the metamaterial properties obtained from the simulation and experimental measurements, indicating the deviation levels from the values predicted by simulation for 80% porosity. In addition, the simulation results for 75%, 70%, and 65% porosity are included.

As observed in Table 5, there are deviations between the simulated and experimental results. Primarily, we noted a decrease in sample porosity. For topology S06, the deviation was 7.62%, while for S08, it was 11.47%. The reason for the porosity deviation lies in the increased thickness of the struts in the metamaterial unit cells. For topology S06, the deviation in strut thickness was smaller than for topology S08, which also resulted in a smaller porosity deviation. It should be noted that strut thickness measurements were taken from the front view. Figure 12 presents the SEM images of the metamaterial samples for each topology, viewed from the side. A significant thickening of the struts in the metamaterial unit cells was observed in the side projection, particularly for the inclined and horizontal struts. On average, the strut thickness in the side projection was 593.64 μm for topology S06 and 477.30 μm for topology S08. Thus, it can be hypothesized that the struts of the unit cells partially exhibit a teardrop-shaped form, which ultimately affects the porosity of the samples. This

Table 4. Properties of metamaterial samples, obtained from compression tests

Topology	Sample	Conditional elastic modulus (GPa)	Conditional yield strength (MPa)	Conditional compressive strength (MPa)	Maximum deformation (%)
S06	Sample 1	5.39	103.60	117.90	5.29
	Sample 2	5.66	102.00	114.95	4.04
	Sample 3	5.53	101.00	114.75	4.32
	Average	5.53	102.20	115.87	4.55
	Standard deviation	0.19	1.13	2.08	0.88
S08	Sample 1	6.36	108.50	130.96	8.57
	Sample 2	6.51	113.50	137.05	9.79
	Sample 3	6.24	109.00	134.89	9.17
	Average	6.44	111.00	134.00	9.18
	Standard deviation	0.11	3.54	4.31	0.86

Table 5. Properties of metamaterial samples, obtained from simulation and experiments

Topology	Sample	Porosity (%)	Strut thickness (μm)	Conditional elastic modulus (GPa)	Conditional yield strength (MPa)	Conditional compressive strength (MPa)
S06	Simulation	80	491	7.22	55.70	67.48
	Experiment	72.38	497.3	5.53	102.20	115.87
	Deviation (%)	7.62	1.29	23.41	45.50	41.76
	Simulation	75	560.5	11.45	77.5	94.63
		70	627	16.59	103.40	123.39
S08	Simulation	80	330	7.46	50.30	69.40
	Experiment	68.53	363.23	6.44	111.00	134.00
	Deviation (%)	11.47	10.07	13.67	54.68	48.21
	Simulation	70	425	15.63	101.70	131.60
		65	470.2	21.24	132.5	169.07

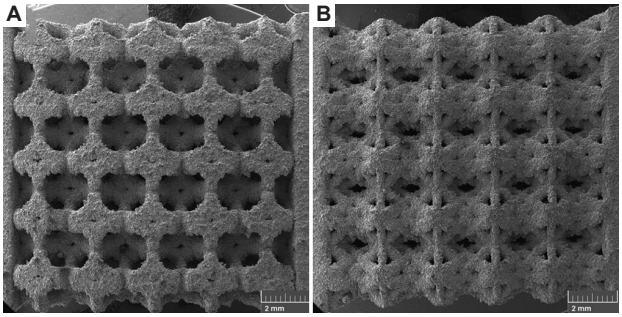

Figure 12. Scanning electron microscopy images of metamaterial samples (side view). (A) S06. (B) S08. Scale bar: 2 mm, magnification: ×18

shape of the unit cell struts has been previously reported in earlier studies.[41] The reasons for this increase in strut thickness lie in the sample orientation during printing and the specific characteristics of the SLM process itself—specifically, the repeated remelting of several underlying layers during sequential scanning of the top powder layer. Unfortunately, the simulation methodology used in this study cannot account for such manufacturing process peculiarities. This naturally leads to deviations in porosity.

In turn, deviations in sample porosity led to deviations in other properties as well. For the Young's modulus of the metamaterial with topology S06, the deviation was 23.41%, while for the metamaterial with topology S08, it was 13.67%. Notably, in both cases, despite the reduced porosity of the experimental samples, the deviation in elastic modulus decreased. The deviation level did not exceed 25% (for the metamaterial with topology S08, it was <15%).

For other properties, a greater level of deviation was observed from the values obtained for 80% porosity. For the metamaterial with topology S06, the deviation in yield strength was 45.5%, and in compressive strength, 41.76%. For the metamaterial with topology S08, the deviation in yield strength was 54.68%, and in compressive strength, 48.21%. At the same time, when comparing the yield strength and compressive strength

values obtained from the simulation at 70% porosity, it can be noted that the difference between experimental and simulated values was minimal. For example, for the metamaterial with topology S08, the experimentally obtained yield strength was 111 MPa, while the simulated value at 70% porosity was 101.70 MPa—a difference of only 9.3 MPa. For metamaterials with topology S06, the difference between the simulated value at 70% porosity and the experimental value for yield strength was even smaller, 1.2 MPa. All this indicates the overall viability of the proposed "simulation-experiment" methodology. Despite some inaccuracies, such as in determining the elastic modulus, the values of other indicators can be effectively predicted by selecting them through modeling for multiple porosity levels.

3.4. Energy absorption characteristics under quasi-static and dynamic compression

This section presents the resulting data on the energy absorption of the investigated metamaterial samples, obtained during both quasi-static compression and dynamic compression (impact testing). Figure 13 shows the force versus crosshead displacement curves obtained from the dynamic testing of the metamaterial samples. Table 6 presents the resulting metrics for each topology.

From Table 6, it can be observed that the SEA for the metamaterial with topology S06 averaged 2.95 J/g, with an average absorbed energy of 7.85 J. For the metamaterial with topology S08, the specific energy absorption was 1.74 J/g, with an average absorbed energy of 5.24 J, which is generally lower than that of topology S06. The results show reasonably good reproducibility.

In addition, the energy absorption parameters of the metamaterial samples were calculated based on the quasi-static compression results. The data are presented in Table 7.

As shown in Table 7, for the metamaterial with topology S06, the SEA during quasi-static compression, which was 2.72 J/g, was comparable to the value obtained under dynamic compression. However, for the metamaterial with topology S08, the opposite trend was observed. Under quasi-static compression, the specific energy absorption was 4.61 J/g, which is more than twice as high as under dynamic compression. The average absorbed energy was 13.83 J, several times higher than the absorbed energy value reported in Du *et al.*[37] This increase in performance is primarily attributed to the ability of metamaterials with topology S08 to undergo gradual failure during quasi-static compression. This allows them to absorb a greater amount of energy during the compression process.

It should be noted that the specific energy absorption for topology S08 is comparable to the results obtained by Zhang *et al.*[40] The cited study investigated a pomelo peel-based topology fabricated from Ti-6Al-4V alloy with different strut cross-sectional geometries. The SEA of the structures by Zhang *et al.*[40] during quasi-static compression ranged from 2.95 to 5.10 J/g. As can be seen, the results for the metamaterial with topology S08 under quasi-static compression are comparable to those from the cited work, indicating the research potential of this topology.

The SEA obtained for the metamaterial with topology S06 (2.72 J/g under quasi-static compression, 2.95 J/g under dynamic compression) is also comparable to the results from Zhang *et al.*[40] However, the values obtained under quasi-static compression were lower than those reported in Zhang *et al.*[7] The reason for this discrepancy may lie in the methodology of the compression-to-failure experiment. In previous studies,[7,40] quasi-static compression tests were conducted until complete compaction and failure of the samples. In our case, to ensure safety compliance and align with standard compression testing practices, the system automatically terminated the experiment when a sharp stress drop exceeding 80% of the maximum achieved

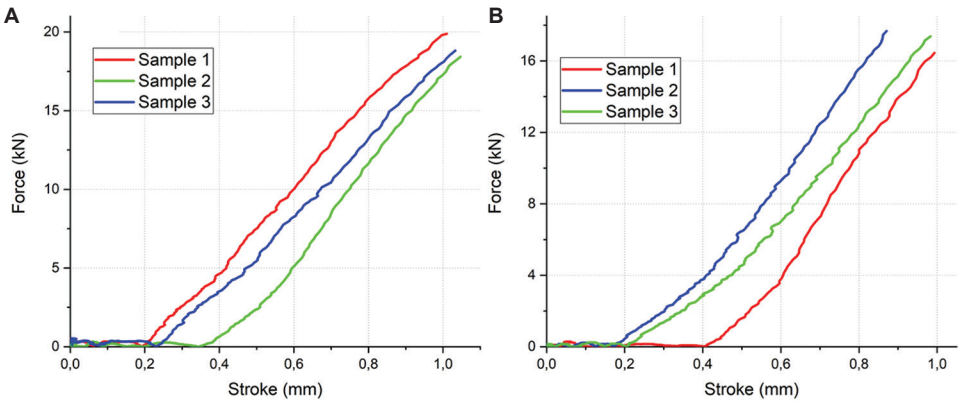

Figure 13. Force-stroke curves of metamaterial samples after dynamic compression tests. (A) Strut_06. (B) Strut_08

Table 6. Energy absorption properties of metamaterial samples, obtained from dynamic compression tests

Topology	Sample	Energy absorption (J)	Specific energy absorption (J/g)
S06	Sample 1	8.35	3.13
	Sample 2	7.36	2.76
	Sample 3	5.96	2.24
	Average	7.85	2.95
	Standard deviation	1.20	0.45
S08	Sample 1	4.45	1.48
	Sample 2	5.36	1.78
	Sample 3	5.90	1.97
	Average	5.24	1.74
	Standard deviation	0.73	0.24

Table 7. Energy absorption properties of metamaterial samples, obtained from quasi-static compression tests

Topology	Sample	Energy absorption (J)	Specific energy absorption (J/g)
S06	Sample 1	8.82	3.31
	Sample 2	5.66	2.13
	Sample 3	6.04	2.27
	Average	7.24	2.72
	Standard deviation	1.72	0.65
S08	Sample 1	12.61	4.20
	Sample 2	15.36	5.12
	Sample 3	13.54	4.51
	Average	13.83	4.61
	Standard deviation	1.40	0.47

value occurred. This approach is more representative for characterizing metamaterials up to the initial failure of their unit cells, but does not evaluate the energy absorption potential during subsequent failure of the remaining intact cells and sample compaction. In future studies, the methodology will be revised to maximize the collection of experimental data.

Furthermore, the obtained SEA values can be compared with results reported for other bioinspired structures. For instance, Guo *et al.*[36] presented a metamaterial with a hierarchical geometry based on the skeleton of the knobby starfish and a triply periodic minimal surface-diamond structure, featuring macrocells of 10 mm and microcells of 2 mm, fabricated using vat photopolymerization. The SEA values of these metamaterials ranged from 0.53 J/g to 2.31 J/g, which are lower than the results for metamaterials with topologies S06 and S08. Similar findings were reported by Khoa *et al.*,[2] who described porous nylon structures with a geometry inspired by the human femoral bone. The SEA values obtained ranged from 1.76 J/g to 2.79 J/g, comparable to the results for topology S06 (under quasi-static compression) but lower than those for topology S08.

In the study by Wang *et al.*,[8] 316L steel metamaterials, designed based on the geometry of a deep-sea sponge skeleton and exhibiting delocalized deformation capability, achieved SEA values under quasi-static compression of approximately 8 J/g, which is higher than those obtained for topology S08. However, it should be noted that this study focused on 2.5D metamaterials, and the cell size was larger (unit cell height: 9 mm). This allowed for the design and successful fabrication of a sufficiently complex geometry capable of delocalized deformation, contributing to the high SEA values.

Thus, such comparisons further demonstrate both the alignment of the research results with the general state of the art and the necessity for further research and modification of the S06 and S08 topologies. This includes refinements from the perspective of the geometries themselves and their unit cell dimensions, to achieve higher SEA values.

4. Conclusion

In this study, metamaterial samples with two types of bioinspired geometries—designed based on the microstructure of pomelo peel (topology S06) and the microstructure of the Japanese rhinoceros beetle's forewing (topology S08)—were fabricated using SLM and validated through experiments. Their mechanical properties were obtained, and energy absorption characteristics were determined under both quasi-static and dynamic compression tests. Based on all the results obtained, the following conclusions can be drawn.

The "simulation-experiment" methodology has proven its effectiveness. Despite deviations in the porosity of the samples during manufacturing, the modeling performed for lower porosity (70%) showed results close to the experimental ones. This confirms the feasibility of using this approach for the initial prediction of metamaterial properties.

The porosity of the fabricated metamaterial samples was 72.38% for metamaterials with topology S06 and 68.53% for metamaterials with topology S08. Deviations from the original models with 80% porosity are associated with powder adhesion to the cell struts, thickening, and changes in the strut geometry during the manufacturing process.

The metamaterial samples with both topologies demonstrated superior mechanical properties compared to structures with similar geometries reported in other scientific studies. For metamaterials with topology S06, the conditional elastic modulus was 5.53 GPa, the conditional yield strength was 102.2 MPa, and the conditional compressive strength was 115.87 MPa. For metamaterials with topology S08, the conditional elastic modulus was 6.44 GPa, the conditional yield strength was 111 MPa, and the conditional compressive strength was 134 MPa.

The SEA of metamaterial samples with topology S06 was 2.72 J/g under quasi-static compression and 2.95 J/g under dynamic compression. For metamaterials with topology S08, SEA was 4.61 J/g under quasi-static compression and 1.74 J/g under dynamic compression. The SEA values of the obtained metamaterials generally align with the results reported in studies by other authors.

The obtained results generally indicate the promising potential of the proposed bioinspired geometries for developing mechanical metamaterials with enhanced energy absorption characteristics. Research in this direction should be continued, including the modification of existing unit cell geometries to achieve higher energy absorption values, the exploration of additional natural geometries for designing new topological variants, and the development of energy-absorbing systems and components based on the acquired data. As a potential direction for modifying the unit cells, one can consider altering geometric elements—specifically the cell bases—to minimize stress concentration at specific points. In addition, it is possible to develop metamaterials based on the presented geometries with a gradient in the porosity of the unit cells or individual cell elements to enhance their strength. Furthermore, to improve the alloy's properties, additional post-processing techniques, such as hot isostatic pressing, could be employed.

Acknowledgments

None.

Funding

This study was supported by the Ministry of Science and Higher Education of the Russian Federation (Agreement No. 075-15-2024-562).

Conflicts of interest

The authors declare that they have no competing interests.

Authors' contributions

Conceptualization: Eduard Farber, Anatoly Popovich
Formal analysis: Eduard Farber
Funding acquisition: Anatoly Popovich
Investigation: Alexey Orlov, Eduard Farber
Methodology: Alexey Orlov
Project administration: Anatoly Popovich
Supervision: Anatoly Popovich
Validation: Alexey Orlov, Eduard Farber
Visualization: Eduard Farber
Writing–original draft: Eduard Farber
Writing–review and editing: Eduard Farber, Alexey Orlov

All authors have read and agreed to the published version of the manuscript.

Ethics approval and consent to participate

Not applicable.

Consent for publication

Not applicable.

Availability of data

The primary data are provided in the paper. Any other raw/processed data required to reproduce the findings of this study are available from the corresponding author on reasonable request.

References

1. Bekele A, Wadee MA, Phillips ATM. Enhancing energy absorption through sequential instabilities in mechanical metamaterials. *R Soc Open Sci*. 2023;10(8):230762.

   doi: 10.1098/rsos.230762

2. Khoa ND, Bohara RP, Ghazlan A, Thai T, Ngo T. Novel hierarchical bioinspired cellular structures with enhanced energy absorption under uniaxial compression. *Aerosp Sci Technol*. 2024;147:108995.

   doi: 10.1016/j.ast.2024.108995

3. Jiang H, Coomes A, Zhang Z, Ziegler H, Chen Y. Tailoring 3D printed graded architected polymer foams for enhanced energy absorption. *Compos Part B Eng*. 2021;224:109183.

   doi: 10.1016/j.compositesb.2021.109183

4. Harish A, Alsaleh NA, Ahmadein M, *et al.* Designing lightweight 3D-printable bioinspired structures for enhanced compression and energy absorption properties. *Polymers (Basel)*. 2024;16(6):729.

   doi: 10.3390/polym16060729

5. Xu S, Chen N, Qin H, Zou M, Song J. Biomimetic study of a honeycomb energy absorption structure based on straw micro-porous structure. *Biomimetics*. 2024;9(1):60.

   doi: 10.3390/biomimetics9010060

6. Bogahawaththa M, Mohotti D, Hazell PJ, Wang H, Wijesooriya K, Lee CK. Energy absorption and mechanical

performance of 3D printed Menger fractal structures. *Eng Struct*. 2024;305:117774.

doi: 10.1016/j.engstruct.2024.117774

7. Zhang Z, Song B, Fan J, *et al*. Design and 3D printing of graded bionic metamaterial inspired by pomelo peel for high energy absorption. *Chinese J Mech Eng Addit Manuf Front*. 2023;2(1):100068.

doi: 10.1016/j.cjmeam.2023.100068

8. Wang P, Yang F, Zheng B, *et al*. Breaking the tradeoffs between different mechanical properties in bioinspired hierarchical lattice metamaterials. *Adv Funct Mater*. 2023;33(45):2305978.

doi: 10.1002/adfm.202305978

9. Zhou Y, Ye L, Chen Y. Developing three-dimensional mechanical metamaterials with tailorable bandgaps for impact mitigation. *J Phys D Appl Phys*. 2024;57(19):195501.

doi: 10.1088/1361-6463/ad2478

10. Jin H, Espinosa HD. Mechanical metamaterials fabricated from self-assembly: A perspective. *J Appl Mech Trans ASME*. 2024;91(4):1-7.

doi: 10.1115/1.4064144

11. Schurger B, Frankovsky P, Janigova S, Bocko J, Kolodziej A. Mechanical metamaterials: Properties and classification. *Acta Mechatronica*. 2023;8(3):29-35.

doi: 10.22306/am.v8i3.98

12. Jiao P. Mechanical energy metamaterials in interstellar travel. *Prog Mater Sci*. 2023;137:101132.

doi: 10.1016/j.pmatsci.2023.101132

13. Jiao P, Mueller J, Raney JR, Zheng X (Rayne), Alavi AH. Mechanical metamaterials and beyond. *Nat Commun*. 2023;14(1):6004.

doi: 10.1038/s41467-023-41679-8

14. Fan J, Zhang L, Wei S, Zheng XR, Alavi AH. A review of additive manufacturing of metamaterials and developing trends. *Mater Today*. 2021;50:303-328.

doi: 10.1016/j.mattod.2021.04.019

15. Kelkar PU, Kim HS, Cho KH, Kwak JY, Kang CY, Song HC. Cellular auxetic structures for mechanical metamaterials: A review. *Sensors (Basel)*. 2020;20(11):3132.

doi: 10.3390/s20113132

16. Ingrole A, Aguirre TG, Fuller L, Donahue SW. Bioinspired energy absorbing material designs using additive manufacturing. *J Mech Behav Biomed Mater*. 2021;119:104518.

doi: 10.1016/j.jmbbm.2021.104518

17. Song J, Yan J, Yi B. Design, fabrication, and characterization of hierarchical mechanical metamaterials. *Front Mech Eng*. 2024;19(1):3.

doi: 10.1007/s11465-023-0776-9

18. Zhang Z, Zhang L, Song B, Yao Y, Shi Y. Bamboo-inspired, simulation-guided design and 3D printing of light-weight and high-strength mechanical metamaterials. *Appl Mater Today*. 2022;26:101268.

doi: 10.1016/j.apmt.2021.101268

19. Gao Z, Ren P, Wang H, Tang Z, Wu Y, Wang H. Additive manufacture of ultrasoft bioinspired metamaterials. *Int J Mach Tools Manuf*. 2024;195:104101.

doi: 10.1016/j.ijmachtools.2023.104101

20. Ma C, Peng X, Zhu D, *et al*. Laser additive manufactured NiTi-based bioinspired helicoidal structure with excellent pseudoelasticity and energy absorption capacity. *J Manuf Process*. 2023;108:610-623.

doi: 10.1016/j.jmapro.2023.11.010

21. Kumar R, Rezapourian M, Rahmani R, Maurya HS, Kamboj N, Hussainova I. Bioinspired and multifunctional tribological materials for sliding, erosive, machining, and energy-absorbing conditions: A review. *Biomimetics (Basel)*. 2024;9(4):209.

doi: 10.3390/biomimetics9040209

22. Siddique SH, Hazell PJ, Pereira GG, Wang H, Escobedo JP, Ameri AAH. On the mechanical behaviour of biomimetic cornstalk-inspired lightweight structures. *Biomimetics (Basel)*. 2023;8(1):92.

doi: 10.3390/biomimetics8010092

23. Lazarus BS, Velasco-Hogan A, Gómez-del Río T, Meyers MA, Jasiuk I. A review of impact resistant biological and bioinspired materials and structures. *J Mater Res Technol*. 2020;9(6):15705-15738.

doi: 10.1016/j.jmrt.2020.10.062

24. Zhang Z, Liu L, Ballard J, Usta F, Chen Y. Unveiling the mechanics of deep-sea sponge-inspired tubular metamaterials: Exploring bending, radial, and axial mechanical behavior. *Thin-Walled Struct*. 2024;196:111476.

doi: 10.1016/j.tws.2023.111476

25. Chao X, Qiwei L, Lu Z, Qingping L, Luquan R. Negative Poisson's ratio metamaterial structure with bionic structure. China, CN116292712. 17 March 2023.

26. Ha NS, Lu G, Xiang X. Energy absorption of a bio-inspired honeycomb sandwich panel. *J Mater Sci*. 2019;54(8):6286-6300.

doi: 10.1007/s10853-018-3163-x

27. Tung CC, Chen YS, Chen WF, Chen PY. Bio-inspired, helically oriented tubular structures with tunable deformability and energy absorption performance under compression. *Mater Des*. 2022;222:111076.

doi: 10.1016/j.matdes.2022.111076

28. Mora A, Palancares-Díaz J, Varela-Soriano J, *et al*. Computational study on the torsional properties of bioinspired tubular metamaterials. *Mech Adv Mater Struct*. 2023;31(26):7767-7776.

    doi: 10.1080/15376494.2023.2249880

29. Tan X, Li Y, Wang L, *et al.* Bioinspired flexible and programmable negative stiffness mechanical metamaterials. *Adv Intell Syst*. 2023;5(6):2200400.

    doi: 10.1002/aisy.202200400

30. Zhijun Z, Guojie C, Kehong W, et al. Anti-explosion energy absorber based on bionic structure. China, CN 117681504. 12 March 2024.

31. Zhang W, Yin S, Yu TX, Xu J. Crushing resistance and energy absorption of pomelo peel inspired hierarchical honeycomb. *Int J Impact Eng*. 2019;125:163-172.

    doi: 10.1016/j.ijimpeng.2018.11.014

32. Zhang X, Han Y, Zhu M, *et al.* Bio-inspired 4D printed intelligent lattice metamaterials with tunable mechanical property. *Int J Mech Sci*. 2024;272:109198.

    doi: 10.1016/j.ijmecsci.2024.109198

33. Mohammadi H, Ahmad Z, Petru M, *et al*. An insight from nature: Honeycomb pattern in advanced structural design for impact energy absorption. *J Mater Res Technol*. 2023;22:2862-2887.

    doi: 10.1016/j.jmrt.2022.12.063

34. Siddique SH, Hazell PJ, Wang H, Escobedo JP, Ameri AAH. Lessons from nature: 3D printed bio-inspired porous structures for impact energy absorption - A review. *Addit Manuf*. 2022;58:103051.

    doi: 10.1016/j.addma.2022.103051

35. Zhou X, Ren L, Song Z, *et al*. Advances in 3D/4D printing of mechanical metamaterials: From manufacturing to applications. *Compos Part B Eng*. 2023;254:110585.

    doi: 10.1016/j.compositesb.2023.110585

36. Guo X, Li X, Wang E, Fuh JYH, Lu WF, Zhai W. Bioinspired hierarchical diamond triply periodic minimal surface lattices with high energy absorption and damage tolerance. *Addit Manuf*. 2023;76:103792.

    doi: 10.1016/j.addma.2023.103792

37. Du Y, Gu D, Xi L, *et al.* Laser additive manufacturing of bio-inspired lattice structure: Forming quality, microstructure and energy absorption behavior. *Mater Sci Eng A*. 2020;773:138857.

    doi: 10.1016/j.msea.2019.138857

38. Zhang Y, Attarilar S, Wang L, Lu W, Yang J, Fu Y. A review on design and mechanical properties of additively manufactured NiTi implants for orthopedic applications. *Int J Bioprinting*. 2021;7(2):15-42.

    doi: 10.18063/IJB.V7I2.340

39. Yuan L, Ding S, Wen C. Additive manufacturing technology for porous metal implant applications and triple minimal surface structures: A review. *Bioact Mater*. 2019;4(1):56-70.

    doi: 10.1016/j.bioactmat.2018.12.003

40. Zhang Z, Song B, Yao Y, *et al*. Bioinspired, simulation-guided design of polyhedron metamaterial for simultaneously efficient heat dissipation and energy absorption. *Adv Mater Technol*. 2022;7(10):2200076.

    doi: 10.1002/admt.202200076

41. Farber E, Orlov A, Popovich A. Auxetic meta-biomaterials: Computer simulation and experimental results. *Metals (Basel)*. 2025;15(3):241.

    doi: 10.3390/met15030241